Supplementary Material

NO photoswitches: single photoinduced linkage isomer in diamagnetic {MNO}^{8} complexes

Artem A. Mikhailov[1], Axel Gansmüller[1], Asma Hasil[1,2], Sébastien Pillet[1], Gennadiy Kostin[3], Guillaume Chastanet[4,5], Theo Woike[1], Dominik Schaniel[1]
[1]Université de Lorraine, CNRS, CRM2, 5400 Nancy, France
[2]Mines St Etienne, Ctr SPIN, UMR CNRS 5307, LGF, 42023 St Etienne, France
[3]Nikolaev Institute of Inorganic Chemistry, Siberian Branch of the Russian Academy of Sciences, 3 Acad. Lavrentiev Avenue, Novosibirsk 630090, Russian Federation
[4]Univ. Bordeaux, CNRS, Bordeaux INP, ICMCB, UMR 5026, F-33600 Pessac, France
[5]CNRS, Institute of Condensed Matter Chemistry of Bordeaux (ICMCB), UPR 9048, France

Synthesis

Powder and single crystalline samples of [Co(fpin)NO(phen)] (**1**) with fpin = perfluoropinacolate(2-) and phen = phenanthroline(0) were provided by T. Riggenmann from LMU Munich, synthesised according to the procedure published in a previous report[1].

X-ray diffraction

The X-ray data were collected on Rigaku Supernova diffractometer with ATLAS CCD detector using a microfocus MoKα X-ray source (λ = 0.71073 Å). CrysAlisPro software package[2] was used both for data collection and reduction. The low temperature during measurements was obtained using liquid helium at 5 K. To measure structural changes in a single crystal Co complex after light irradiation, first, the structure was measured in GS at 5 K. Irradiation of the single crystal was performed *in-situ* on the diffractometer at 5 K with 590 nm LED with 30 mW optical power for 30 min before data collection. During these first 30 min of irradiation the crystal was rotated around the axis perpendicular to the light beam to ensure a homogenous distribution of the photoproduct in the whole crystal volume. The LED light was left on the sample during all the data collection to ensure constant population of the PLI. The measured structures have been deposited with the CCDC with deposition numbers 2448993 and 2448997 for GS and PLI, respectively. Crystal data and refinement details for reported structures are shown in Table S1. The crystal structures of the ground state (GS) and the photoinduced linkage isomer (PLI) were solved using ShelXT.[3] All structures were refined by means of ShelXL[4] implemented in Olex2.[5] The superposition of GS and PLI in the photoexcited crystals was refined based on Fourier difference map of given structure and photodifference map calculated between respective PLI and GS observed structure factors (F_{obsPLI}-F_{obsGS}).[6] In all crystal structures all non-hydrogen atoms were refined anisotropically. The hydrogen atoms positions were constrained and treated as riding rotating groups. The GS structure before irradiation was refined without any restrains. The structure after irradiation was refined with disorder of the NO ligand over two positions: NO_{GS} and ON_{PLI}. The ON_{PLI} part was refined with restraint on atomic displacement parameters of both N and O (ISOR, see below) to avoid non-positively defined ellipsoids. The NO_{GS} part was refined using DFIX, DANG and ISOR, since the angle and bond lengths of Co-N-O linkage of GS are known from the measurement before irradiation. Thus, the bonds Co-N and N-O of the Co-N-O linkage of the GS part were constrained by DFIX to 1.83 Å and 1.161 Å, respectively. The angle Co-N-O was

constrained to 2.636 using DANG. ISOR (0.001; 0.0005) was applied to both N and O atoms of NO_{GS}, along with EADP for pairs $N1_{GS}$, $O1A_{PLI}$ and $O1_{GS}$, $N1A_{PLI}$.

Table S1. Crystal data and refinement details of studied structures.

Identification code	[Co(fpin)NO(phen)] GS	[Co(fpin)NO(phen)] PLI
Empirical formula	$C_{18}H_8CoF_{12}N_3O_3$	$C_{18}H_8CoF_{12}N_3O_3$
Formula weight	601.20	601.20
Temperature/K	5.0	5.0
Crystal system	triclinic	triclinic
Space group	P-1	P-1
a/Å	8.4918(4)	8.5175(3)
b/Å	8.7777(4)	8.8128(4)
c/Å	13.2804(6)	13.3093(5)
α/°	94.784(4)	94.496(3)
β/°	90.250(4)	90.168(3)
γ/°	93.681(4)	93.578(3)
Volume/Å^3	984.37(8)	993.98(7)
Z	2	2
ρ_{calc}g/cm^3	2.028	2.009
μ/mm^{-1}	1.015	1.005
F(000)	592.0	592.0
Crystal size/mm^3	0.35 × 0.23 × 0.16	0.35 × 0.23 × 0.16
Radiation	Mo Kα (λ = 0.71073)	Mo Kα (λ = 0.71073)
2Θ range for data collection/°	4.666 to 64.976	4.646 to 65.73
Index ranges	-12 ≤ h ≤ 12, -13 ≤ k ≤ 13, -19 ≤ l ≤ 18	-12 ≤ h ≤ 12, -13 ≤ k ≤ 13, -19 ≤ l ≤ 18
Reflections collected	20274	21438
Independent reflections	6425 [R_{int} = 0.0420, R_{sigma} = 0.0491]	6759 [R_{int} = 0.0651, R_{sigma} = 0.0708]
Data/restraints/parameters	6425/0/334	6759/15/341
Goodness-of-fit on F^2	1.070	1.147
Final R indexes [I>=2σ (I)]	R_1 = 0.0401, wR_2 = 0.0883	R_1 = 0.0666, wR_2 = 0.1279
Final R indexes [all data]	R_1 = 0.0587, wR_2 = 0.1006	R_1 = 0.0795, wR_2 = 0.1356
Largest diff. peak/hole / e Å^{-3}	0.73/-0.74	1.14/-1.50

Table S2. Experimental X-ray diffraction (Exp.) and calculated (Calc., DFT optimised structures (ADF) used for UV/vis absorption spectra calculation) chosen bond lengths and angles.

	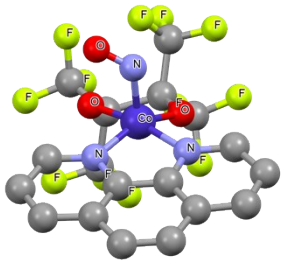		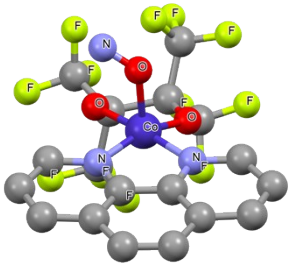	
Bond length [Å]	GS		PLI	
	Calc.	Exp.	Calc.	Exp.
Co-NO	1.787	1.8299(17)	-	-
Co-ON	-	-	1.951	1.986(5)
N-O	1.174	1.161(2)	1.162	1.163(5)
$Co\text{-}O_{fpin}$	1.837; 1.869	1.8666(13); 1.8736(13)	1.830; 1.863	1.867(2); 1.874(2)
$Ru\text{-}N_{phen}$	1.949; 1.910	1.9488(16); 1.9388(16)	1.915; 1.901	1.941(2); 1.938(2)
Angle [°]	Calc.	Exp.	Calc.	Exp.
Co-N-O	123.6	121.99(14)	-	-
Co-O-N	-	-	126.1	123.1(3)

IR-spectroscopy

IR measurements were performed at different temperatures between 10 and 300 K and the sample was kept in a vacuum inside a closed cycle cryostat, using a Nicolet 5700 FT-IR spectrometer with a resolution of 1 or 2 cm^{-1}. The sample was ground, mixed with KBr and pressed into pellets. The KBr pellets were bonded onto the cold finger of the Oxford Optistat cryostat using silver paste, and irradiated through KBr windows with LED or LASER light in the wavelength range of 365-1300 nm. Fig. S1 exemplarily shows the infrared spectrum in the range 400-2000 cm^{-1}, before (solid black line) and after irradiation with light of a 589 nm LASER (solid red line). The most pronounced changes occur at the NO stretching mode (see main text). To investigate the isothermal kinetics during the decay of PLI to GS the following protocol was applied: on the first stage the sample was irradiated at 10 K using 590 nm light from an LED (30 mW optical power) in order to generate PLI; then the temperature was increased up to a chosen value (55, 58, 60 or 65 K) and then IR spectra were measured periodically in isothermal mode. The decay constants k were calculated from the decrease in the area of $\tilde{\nu}(ON)_{PLI}$ band at 1780 cm^{-1}. The obtained experimental data were approximated using the equation of a first-order decay $A=A_0 \cdot \exp(-k \cdot t)+A_\infty$ (see Fig. S2). Using the decay constants k determined at each measured temperature T, the activation energy E_A and frequency factor k_0 were determined in Arrhenius coordinates $k=k_0 \cdot \exp(-E_A/(R \cdot T))$, where R is the molar gas constant. The conditions for optimal population were explored by varying the irradiation wavelength over a wide spectral range (see Fig. S3) using both CW and pulsed light sources and by studying the population as a function of exposure Q (Jcm^{-2}) as discussed in the main text. **Kinetics measurements were conducted using a 0.5 mm thick polyethylene (PE)**

filter blocking IR-light partially above 1400 cm^{-1} to reduce the exposure of the sample to the light of the IR-spectrometer (see main text). The measurement time per population step was set to 10 s in order to further reduce sample exposure to the IR-beam of the spectrometer. Under the same conditions with the PE filter, a PLI population change of 8% was observed after 5 min of sample exposure to the IR-spectrometer beam. Hence, for a 10 s exposure we estimate a population loss of 0.25% due to the IR-light of the spectrometer, which is within the error of the population determination. We therefore are confident that under these conditions the IR-beam of the spectrometer did not affect the kinetics measurements.

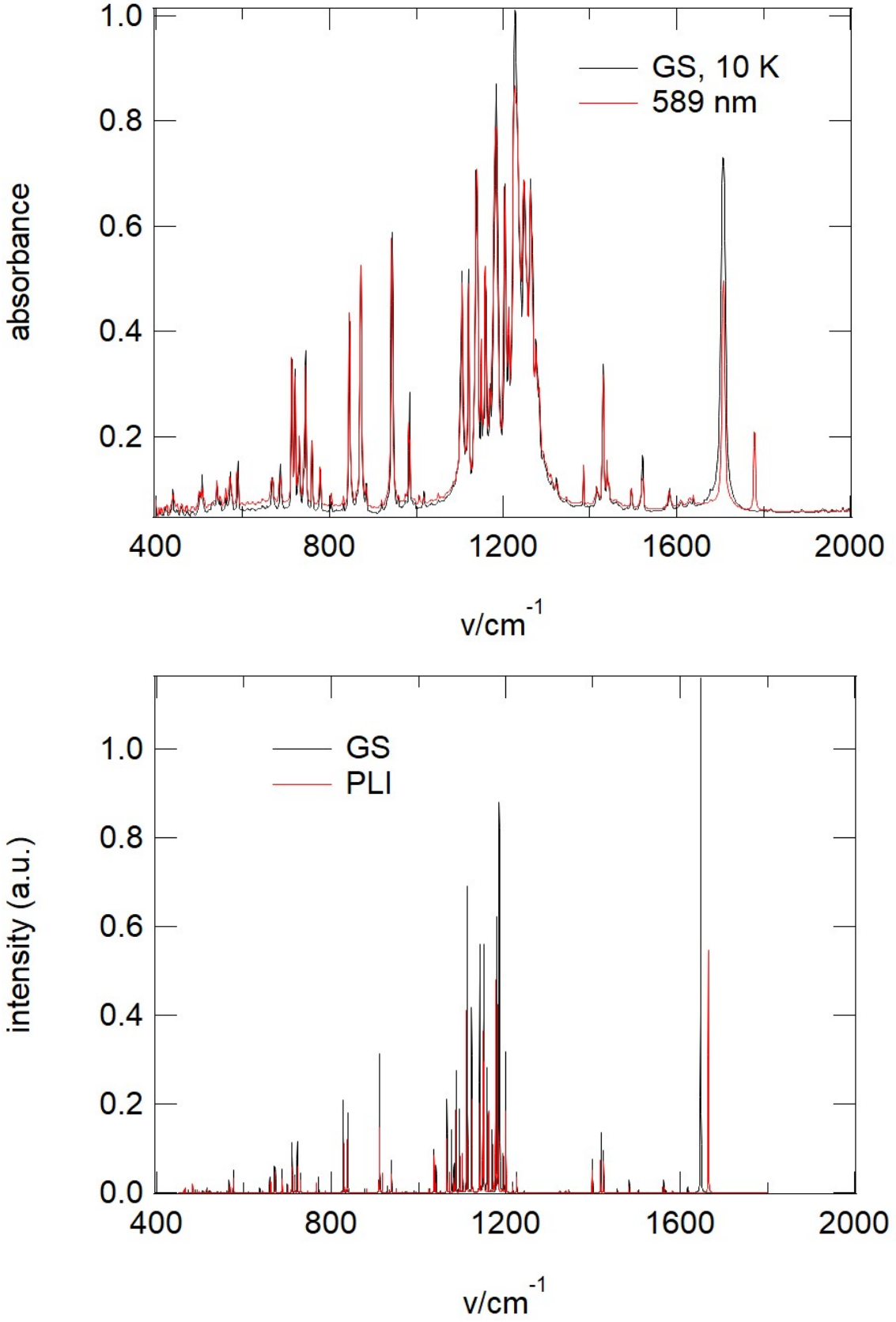

Fig. S1. (top) Infrared spectrum of (**1**) at 10 K in the range 400-2000 cm^{-1}, before (solid black line) and after irradiation with 589 nm LASER light (solid red line). (bottom) Calculated (CASTEP) IR spectra for GS (black) and PLI (red).

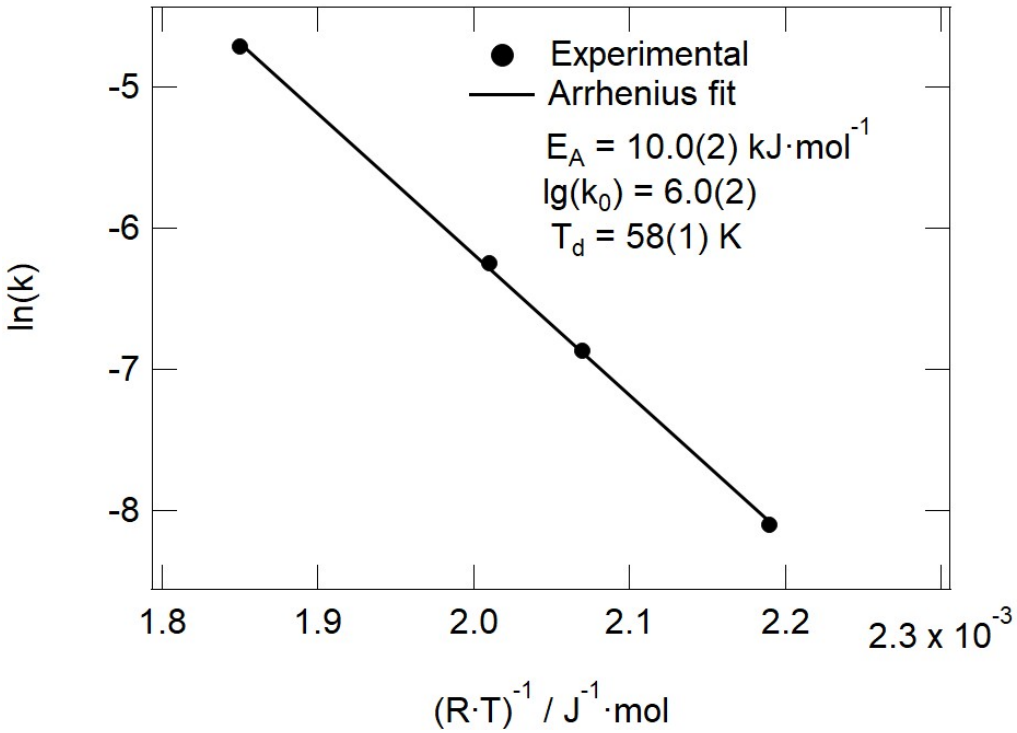

Fig. S2. Arrhenius plot of PLI to GS thermal relaxation.

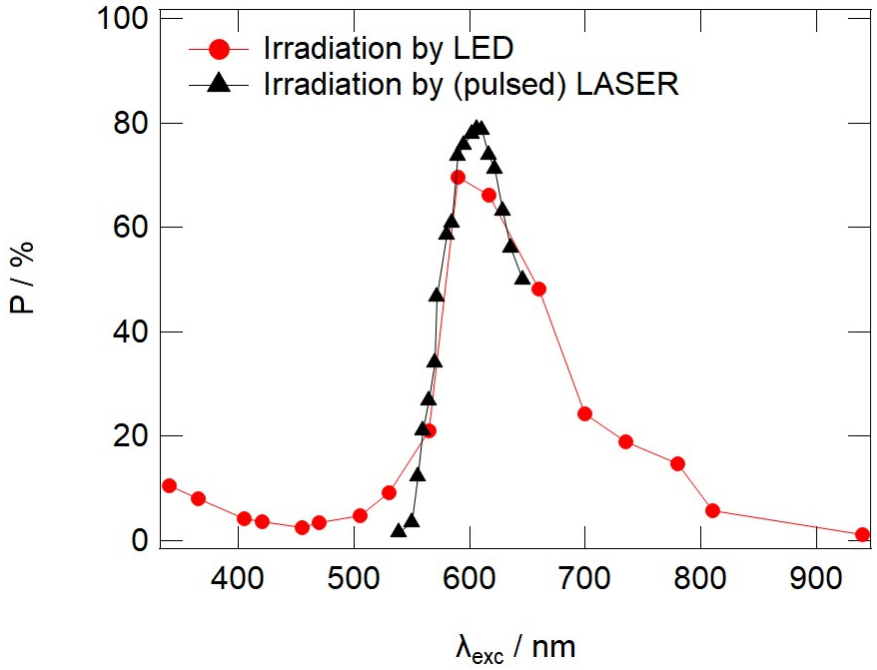

Fig. S3. Wavelength dependent population (at saturation) with the maximum at 606 nm.

UV-VIS absorption spectroscopy

UV-Vis measurements were performed using both, a Shimadzu UV-3600 spectrometer and a Varian Cary 4000 spectrometer, with a resolution of 2 nm at 10 K. For both experiments, polycrystalline samples were prepared as KBr pellets like for IR spectroscopy for measuring solid-state spectra in transmission mode. Likewise, the irradiation procedure was produced

in the same manner as during the infrared spectroscopy experiments. Fig. S4 shows the results before and after photoirradiation as well as the difference spectra. Fig. S5 shows the fit with a Gaussian peak to the band at 1100 nm.

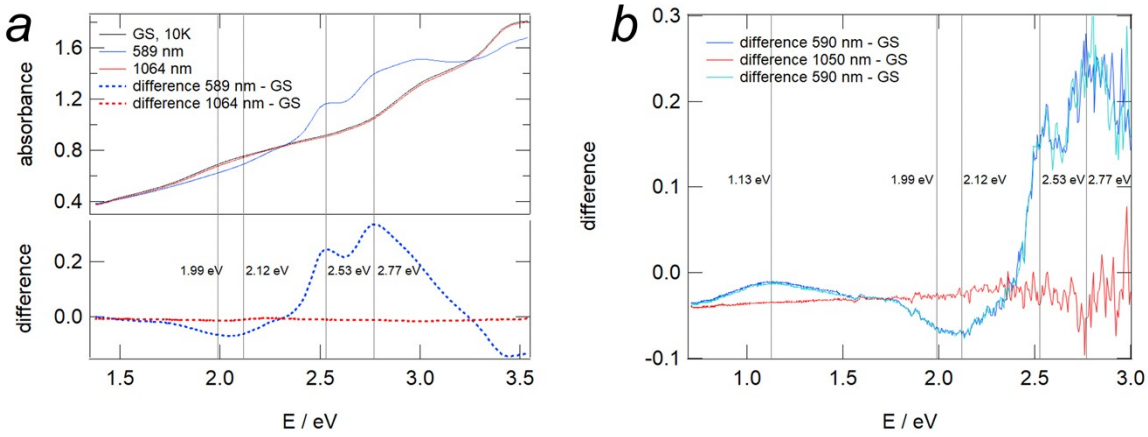

Fig. S4: Solid-state absorption spectra of (**1**) in GS and after generation of PLI with 589 nm light and erasure of PLI with infrared (1064 nm) light at 10 K. (a) low concentration of (**1**) in KBr pellet for measurement in the range up to 3.5 eV, bottom curves show the difference between irradiated and non-irradiated sample. (b) difference spectra for a higher concentration of (**1**) in KBr to enable measurement of weak absorption bands in the near infrared spectral range. Numbers indicate peak positions in the difference spectra.

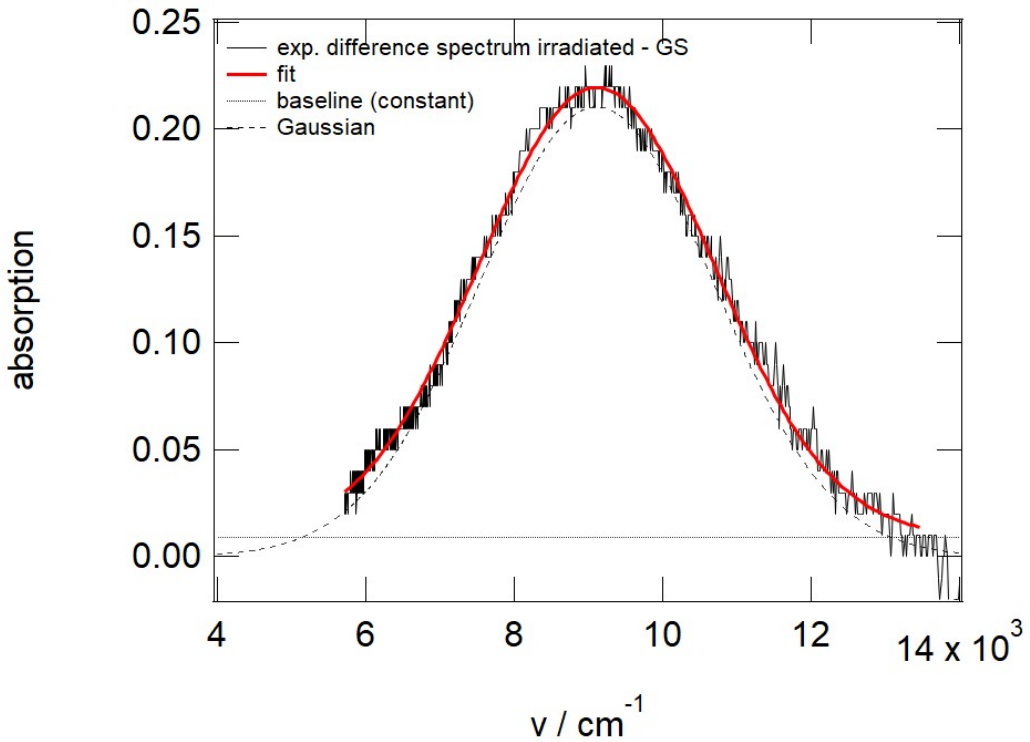

Fig. S5. Fit of the absorption band at about 1100 nm obtained from the difference spectra irradiated – non-irradiated sample. The fit with a single Gaussian peak yields a peak position of 9109(5) cm^{-1} and a FWHM of 2237(13) cm^{-1}.

Quantum yield calculations

GS to PLI (590 nm)

Quantum yield (Φ) of GS→PLI transformation was estimated using the formula considering only the initial linear part of X_{GS} kinetics (X_{GS} is molar fraction of GS):

$$\Phi = \frac{k_{fit} N(GS)_0}{I_0(1 - 10^{-A_{ex}})},$$

where k_{fit} [J^{-1}] is the slope dX_{GS}/dE_{laser} of the initial linear part of the graph (0.16535 J^{-1}) (E_{laser} - total pulsed energy arrived on the sample [J] : 10 $mW_{(light\ power)}$/0.64$cm^2_{(area\ of\ the\ detector)}$·1.33$cm^2_{(area\ of\ the\ sample)}$=20.78 mJ/s), $N(GS)_0$ [mol, $1.5968 \cdot 10^{-6}$] initial quantity of GS molecules, I_0 [$mol \cdot J^{-1}$] is the energy of 1 mol of 410 nm photons calculated by the formula:

$$I_0 = \frac{\lambda_{ex}}{hcN_a},$$

where λ_{ex} [m] is the wavelength of the pulsed laser, h is the Plank constant [J·s], c [$m \cdot s^{-1}$] is the speed of light, and N_a [mol^{-1}] is the Avogadro number. A_{ex} is the absorbance of the sample at the excitation wavelength:

$$A_{ex} = \varepsilon_{ex} C_0 l_{ex},$$

where ε_{ex} [$L \cdot mol^{-1} \cdot cm^{-1}$] is the absorption coefficient of GS at 590 nm, C_0 [$mol \cdot L^{-1}$] is the initial concentration of GS molecules, l_{ex} [cm] it the path length of the laser light through the sample (thickness of the sample).

Thus,

$$A_{ex} = 262.01 \cdot 0.03 \cdot 0.04 = 0.31,$$

$$I_0 = \frac{590 \cdot 10^{-9}}{6.62 \cdot 10^{-34} \cdot 3 \cdot 10^8 \cdot 6.02 \cdot 10^{23}} = 4.93 \cdot 10^{-6}\ mol \cdot J^{-1},$$

$$\Phi = \frac{0.16 \cdot 1.6 \cdot 10^{-6}}{4.93 \cdot 10^{-6} \cdot (1 - 10^{-0.31})} = 0.10\ or\ 10(1)\%.$$

PLI to GS (1050 nm)

Quantum yield (Φ) of PLI→GS transformation was estimated using the formula considering only the initial linear part of X_{PLI} kinetics (X_{PLI} is molar fraction of PLI):

$$\Phi = \frac{k_{fit} N(PLI)_0}{I_0(1 - 10^{-A_{ex}})},$$

where k_{fit} [J^{-1}] is the slope dX_{GS}/dE_{laser} of the initial linear part of the graph (1.80 J^{-1}) (E_{laser} - total pulsed energy arrived on the sample [J]: 1 $mW_{(light\ power)}/0.64cm^2_{(area\ of\ the\ detector)} \cdot 1.33\ cm^2_{(area\ of\ the\ sample)}$ = 2.0781 mJ/s), $N(PLI)_0$ [mol, $1.07 \cdot 10^{-6}$] initial quantity of PLI molecules, I_0 [$mol \cdot J^{-1}$] is the energy of 1 mol of 1050 nm photons calculated by the formula:

$$I_0 = \frac{\lambda_{ex}}{hcN_a},$$

where λ_{ex} [m] is wavelength of pulsed laser, h is Plank constant [J·s], c [$m \cdot s^{-1}$] – speed of light, N_a [mol^{-1}] is Avogadro number. A_{ex} is absorbance of the sample at excitation wavelength:

$$A_{ex} = \varepsilon_{ex} C_0 l_{ex},$$

where ε_{ex} [$L \cdot mol^{-1} \cdot cm^{-1}$] is absorption coefficient of PLI at 1050 nm, C_0 [$mol \cdot L^{-1}$] is initial concentration of PLI molecules, l_{ex} [cm] – length of the light of the laser path through the sample (thickness of the sample).

Thus,

$$A_{ex} = 131.01 \cdot 0.020 \cdot 0.04 = 0.10,$$

$$I_0 = \frac{1050 \cdot 10^{-9}}{6.62 \cdot 10^{-34} \cdot 3 \cdot 10^8 \cdot 6.02 \cdot 10^{23}} = 8.78 \cdot 10^{-6}\ mol \cdot J^{-1},$$

$$\Phi = \frac{1.80 \cdot 1.07 \cdot 10^{-6}}{8.78 \cdot 10^{-6} \cdot (1 - 10^{-0.10})} = 1.07\ or\ 107(19)\%.$$

DFT and TD-DFT calculations for XAS and UV/Vis spectra

Density functional theory (DFT) calculations of X-ray absorption (XA) spectra were performed with the ADF 2022 package.[7] For the geometry optimization of [Co(fpin)(NO)(phen)] in GS and PLI (closed-shell electron configurations) in the gas phase, the Perdew-Burke-Ernzerhof (PBE) functional[8] with quadruple-ζ-quality with 4 polarization functions all-electron (QZ4P) basis set[9] was used. Initial geometries for the structure optimization were taken from experimental X-ray diffraction data. Comparison of experimental and calculated structural data is given in Table S2. To gather information on the composition of molecular orbitals involved in the main excitations, molecular orbitals were calculated for optimised structures on the same level of theory with a scalar relativistic effects.[10] XA spectra of Co K-edge of GS and PLI were calculated

on the same level of theory. XA spectra were simulated using time-dependent DFT (TD-DFT) approach for allowed transitions by the Davidson method.[11] The first 100 singlet-singlet electronic excitations were calculated. Natural transition orbitals (NTOs) were calculated for representation of the transitions.[12]

The version 5.0 of Orca package[13]was used to perform TD-DFT calculations of UV-Vis spectra. Geometry optimization and spectra calculations were carried out in gas phase using B3LYP functional.[14] All atoms were described by def2-TZVP basic set[15]. The zero-order regular approximation (ZORA)[16] was incorporated to consider the scalar relativistic effect.

UV/Vis spectra

The TD-DFT calculations of UV-Vis spectra for a gas phase molecule in GS and PLI give the oscillator strengths and transition energies from which we can assign the relevant HOMO – LUMO transitions (see Fig. S6). Calculated spectra are shifted about 100 nm with respect to experimental ones. For example, the band at 600 nm in experimental GS spectrum can be found at 700 nm in calculated spectrum of GS. Yet, the main features observed in the experiment (smaller PLI absorption at 600 nm and corresponding higher absorption at 450 nm) can be found in the calculated spectra. The broad band at 700 nm in the DFT spectrum of GS is represented by the three strongest excitations at 768.5, 661.2 and 637.8 nm with oscillator strengths of $2.5\cdot10^{-3}$, $5.2\cdot10^{-3}$ and $1.7\cdot10^{-3}$, respectively. These excitations consist of several transitions, the most abundant ones are HOMO-1 → LUMO+3, HOMO-2 → LUMO+3 and HOMO → LUMO, respectively. The average occupancies of these HOMOs are Co(36.1%), NO(34.7%), L(29.2%), and LUMOs - Co(11.9%), NO(13.4%), L(74.7%). Thus, according to TD-DFT, the experimental GS band at 600 nm can be described as mixed metal and ligand centered to ligand (largely to phen ligand) transition. According to calculations, PLI possess three bands in this range – 684, 676 and 662.8 nm, corresponding to HOMO → LUMO, HOMO-3 → LUMO+1 and HOMO → LUMO+3, respectively. Oscillator strengths of these transitions are $1.3\cdot10^{-3}$, $1\cdot10^{-3}$ and $1\cdot10^{-3}$, respectively. In PLI, the average occupancies of these HOMOs are Co(43%), NO(31.5%), L(25.5%), and LUMOs - Co(11.7%), NO(15%), L(73.3%). As can be seen, the orbital composition in GS and PLI around 600 nm does not change significantly, meaning that the gain of PLI population in case of 590 nm excitation is due to the significant decrease in absorption around 600 nm in PLI, but not due to the change of the nature of excited orbitals. At least three experimentally observed PLI bands at 500, 460 and 420 nm can be assigned to the three the most intense calculated excitations at 510.1, 470.8 and 457.4 nm, respectively. These excitations correspond to HOMO-1 → LUMO+6, HOMO-2 → LUMO+1 and HOMO-3 → LUMO transitions, with oscillator strengths of $1.2\cdot10^{-3}$, $7.7\cdot10^{-2}$ and $3.7\cdot10^{-2}$, respectively. In average all these transitions correspond to Co(46.4%), NO(1.2%), L(52.4%) → Co(8.9%), NO(3.4%), L(87.7%) occupancies. Concerning the lowest lying transition observed in the experiment (at 1100 nm), which is responsible for the depopulation of the PLI, the calculation delivers three potential transitions at 2089 nm, 1324 nm, and 1072 nm. The two latter ones have significant contributions from the HOMO-1 and HOMO-2 (metal-d) to LUMO+2 (ligand centered orbital with significant NO contribution).

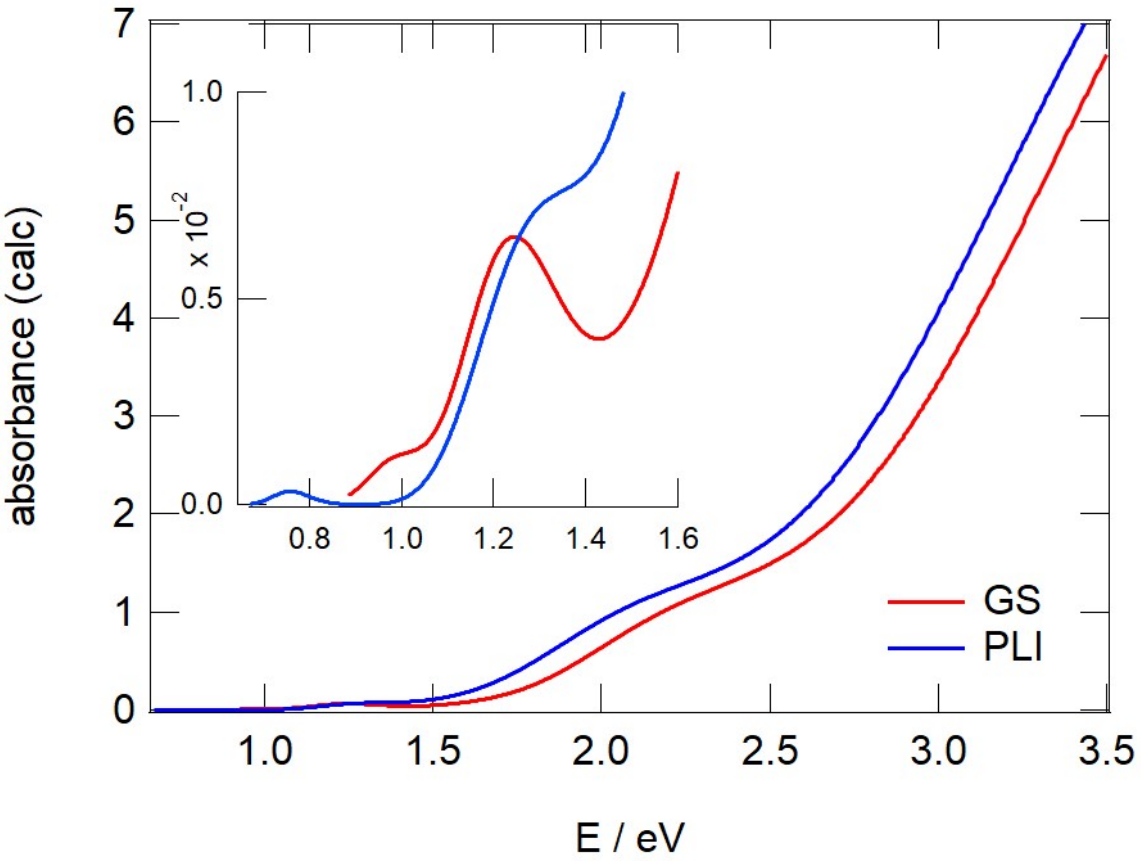

Fig. S6: TD-DFT calculated UV-Vis spectra of GS (red) and PLI (blue). The insert shows the low-energy range (0.67-1.6 eV) in order to highlight the low-lying transitions.

X-ray absorption spectroscopy

The X-ray absorption (XA) spectra at Co K-edges were measured at the LUCIA beamline of Synchrotron SOLEIL (Saint-Aubin, France),[17,18] with a nominal energy of 2.3 GeV and current ring of 500 mA. The sample was pressed as a pellet diluted in polyethylene and glued onto a copper holder with conductive silver paste. The holder was placed in a vacuum chamber on a cryostat cooled down to 30 K. The X-ray beam energy was selected using a Si(111) double crystal monochromator and XA spectra were collected in total fluorescence yield mode ($L_{\alpha 1}$ emission line) using a silicon drift detector from Bruker. The spectra were measured in the range of 7620-8000 eV. The resolution of 0.3 eV was applied for the range of 7700-7740 eV, lower resolution (0.5-2 eV) was applied for other ranges. To produce the PLI isomer the sample was irradiated with the same 590 nm LED of 30 mW optical power for 45 min at 30 K, which was used for the IR, UV-Vis and XRD experiments.

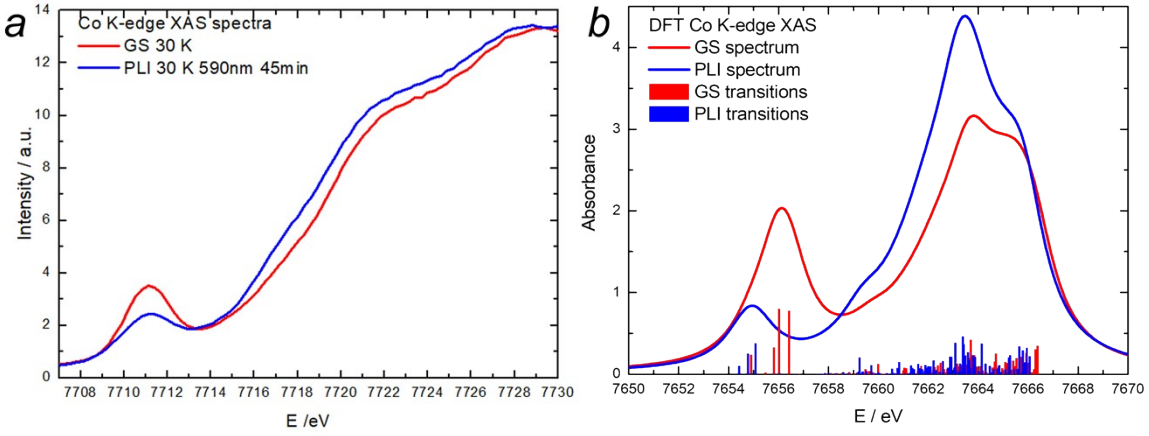

Fig. S7: Measured (a) Co K-edge X-ray absorption spectra before (blue) and after (red) irradiation with λ = 590 nm at T = 30 K. Calculated (b) Co K-edge TD-DFT XA spectra of GS and PLI. The vertical bars represent the transition probabilities (oscillator strengths). Calculation was performed with 100% PLI population.

In the Co K-edge XA spectra (7700 - 7750 eV range) we have detected a strong pre-edge peak at 7711.1 eV and three main broad peaks around 7718, 7722 and 7729 eV shown in Fig. S7a for GS (blue) and PLI (red). The generation of PLI (λ = 590 nm, T = 30 K) induces a decrease in the area of the pre-edge peak and corresponding increase in the main peaks shown in Fig. S7a. The intensity of the pre-edge peak depends on the local symmetry of the complex, where a higher symmetry generally results in a lower intensity of the pre-edge peak. For instance, the four-fold coordinated complex [Co(salen)] has a lower pre-edge peak intensity compared to the five-coordinated nitrosyl complex [Co(salen)NO].[19] The lower local symmetry allows more efficient mixing of metal and ligands' orbitals thereby increasing the pre-peak intensity. Ligand structure change also can influence the intensity of pre-peak, as it was shown in [Co(L)NO] complexes with different porphyrin ligands L.[20] Since in our case neither the local symmetry of the complex nor the ligand composition change when going from GS to PLI, we used DFT calculation to further investigate the origin of the observed experimental XA features.

In order to understand which transitions are responsible for XA changes after irradiation, we have calculated TD-DFT XA spectra (ADF package, see above) for a molecule in gas phase in GS and PLI (see Fig. S7b). The pre-edge peak of GS (red) is composed of the four strongest Co 1s transitions with different oscillator strengths of $2.3 \cdot 10^{-5}$, $3.2 \cdot 10^{-5}$, $8 \cdot 10^{-5}$ and $7.7 \cdot 10^{-5}$. Their transition energies are 7654.9 eV, 7655.8 eV, 7656.0 eV and 7656.4 eV, respectively. The compositions of lowest unoccupied molecular orbitals (LUMOs) involved in these transitions are: 7654.9 eV: Co(1s) → Co(1.5%), NO(11.1%) and the rest ligands L(72.9%) [LUMO]; 7655.8 eV: Co(1s) → Co(52.0%), NO(5.8%), L(24.1%) [LUMO+3]; 7656.0 eV: Co(1s) → Co(23.1%), NO(20.8%), L(44.3)% [LUMO+4]; 7656.4 eV: Co(1s) → Co(17.8%), NO(26.2%), L(42.0%) [LUMO+5]. The percentages show the orbital contributions of Co(s, p, d), N(s, p) and L(s, p). Neglecting the quadrupolar contribution, the main contributions to these transitions come from allowed 1s → np dipole transitions, which explains the strength of the pre-edge peak. Due to the different compositions of the unoccupied orbitals, we do not discuss the crystal field behaviour of the central Co(I) atom. In PLI there are only the three strongest transitions: 7654.4 eV: Co(1s) → Co(3.7%), NO(82.1%) [LUMO]; 7654.8 eV: Co(1s) → Co(18.6%),

NO(20.1%), L(46.1%) [LUMO+1]; 7655.1: Co(1s) → Co(29.1%), NO(46.4%), L(13.4%) [LUMO+3]. The oscillator strengths of these transitions are $9.9 \cdot 10^{-6}$, $2.5 \cdot 10^{-5}$ and $3.7 \cdot 10^{-5}$, respectively, which are significantly lower compared to GS. The area of the pre-edge peak decreases in PLI, due to the fact that the average occupation of Co and L decreases (from $23.6\%_{GS}$ and $45.8\%_{GS}$ to $17.6\%_{PLI}$ and $19.8\%_{PLI}$, respectively), and average NO occupation increases (from $16.0\%_{GS}$ to $49.5\%_{PLI}$), which results in a smaller transition probability (oscillator strength). The transitions in PLI are shifted to lower energies (shift by -1.4 eV, -1.2 eV, -1.3 eV), which results in a shift of the PLI peak by 1.2 eV to lower energy. The systematically lower transition energies of excitations attributed to the PLI pre-edge peak demonstrate that LUMOs of PLI possess lower energies compared to those of GS, since the Co(1s) orbital is almost unaffected by the N-O rotation (-7586.4 eV in GS and -7586.1 eV in PLI). At higher energies there are much more transitions (see Fig. S7b) which increase in PLI, as also detected in the experiment.

Magnetic measurements

The measurements have been performed on a Quantum Design MPMS 7XL SQUID Magnetometer. For bulk magnetization measurements 12.1 mg of [Co(fpin)NO(phen)] have been prepared using the standard procedure (sample in a polyethylene bag whose diamagnetic contribution is known). For the photomagnetic measurements a much smaller amount of sample, between 10 and 50 times less, was used and prepared as a thin layer on Kapton tape to ensure a good penetration of light into the powder. Light irradiation was performed using various wavelengths, 650 nm and 589 nm from LASERs, and 590 nm from LED as in the other experiments, and the light was introduced via an optical fiber in the magnetometer.

On the bulk measurement (Fig. S8) there is a clear paramagnetic signal, very weakly anisotropic. The « straight line » character of the $\chi_M T$ curves is quite characteristic of temperature-independent paramagnetism (TIP). TIP stems from the coupling of the diamagnetic ground state with excited states close enough in energy to be mixed by the application of a magnetic field. However, one would expect also a straight line in the magnetization curves, which is not the case. So the signal most probably does not come from the TIP of the Co(I) ion but more from a Co(II) impurity. A pure S = 3/2 Co(II) ion is expected to have a $\chi_M T$ value at room temperature of around 2.5 cm^3K/mol and a magnetization saturation around 3. So we could expect around 2-10 % of Co(II) impurity.

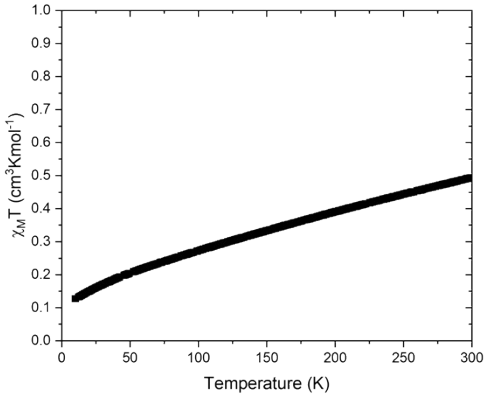

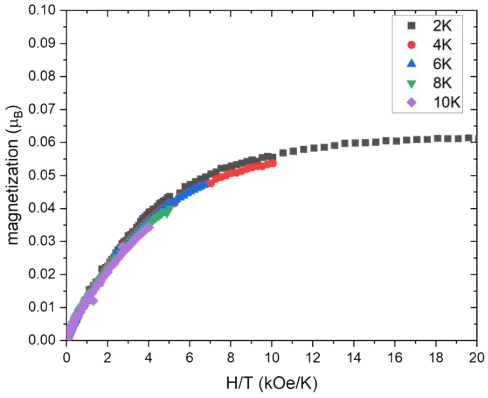

Fig. S8: Bulk magnetization a) as a function of temperature using an applied magnetic field of H=10kOe and b) as a function of applied magnetic field for 5 different temperatures.

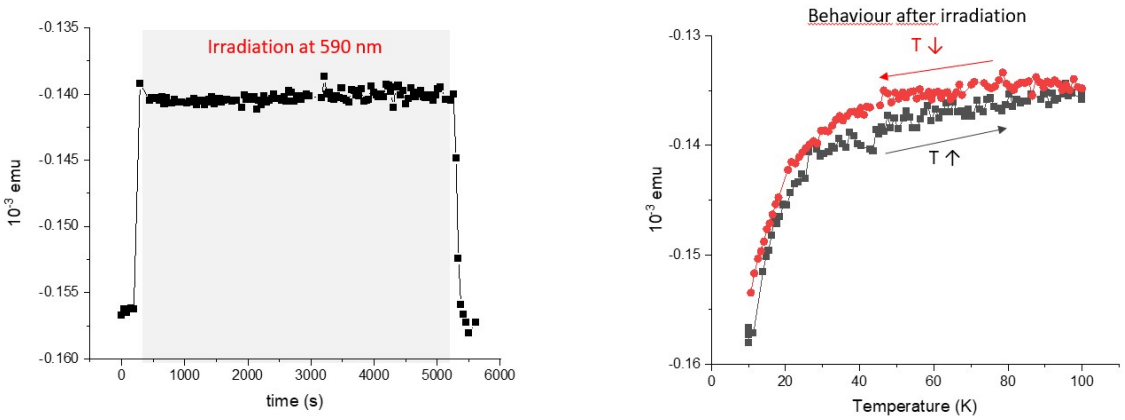

Fig. S9: Effect of light irradiation on diamagnetic signal of (**1**). a) Evolution of signal from start to end of irradiation at 10 K. b) Temperature scan after switching of the light.

The results of the photomagnetic measurements are shown in Fig. S9. The increase in the magnetisation value under the application of the light irradiation is due to the heating it provokes. This is confirmed by the fact that 1) under irradiation the magnetisation value does not change, 2) the value before and after irradiation are strictly identical and 3) the thermal dependence of the magnetisation is exactly the same after irradiation and after the expected relaxation of the photo-induced state.

Solid-state calculations (CASTEP)

Infrared spectra and charge density were calculated using density functional theory (DFT) after performing geometry optimization starting from the X-ray diffraction models. We used the first principle quantum mechanical code CASTEP19.11[21,22] considering the Perdew–Burke–Ernzerhof generalised gradient approximation (PBE),[23] with ZORA relativistic treatment.[24] The structures were described as extended solids using periodic boundary conditions. The wavefunctions were expanded using a planewave (PW) basis set with a kinetic energy cutoff and Brillouin zone k-point spacing chosen to produce converged results. In a first step, geometry optimization of all atoms was performed, as already successfully applied in a previous paper.[25] For geometry optimization, IR spectra, and charge density calculations, the Norm Conserving pseudopotentials CASTEP 19.0 (NCP19) were used to describe the interaction of the valence electrons with the nuclei and core electrons. The wavefunctions were expanded using a PW basis set with a kinetic energy cutoff of 900 eV and integration over the Brillouin zone with k-point spacing of 0.04 $Å^{-1}$ on the Monkhorst–Pack (MP) mesh.[26] The sizes of the standard and fine grids were set to 2 and 3 respectively. The self-consistent field calculations were considered to be converged when the total energy of the system was stable within 10^{-10} eV. Geometry optimization was performed with semi-empirical dispersion correction using the Tkatchenko–Scheffler scheme.[27] The geometry optimization was performed with strict convergence tolerance criteria (10^{-7} eV per atom total energy convergence; $5 \cdot 10^{-3}$ eV per Å max ionic force; and $5 \cdot 10^{-4}$ Å max ionic displacement). Results of relevant calculated atomic distances and angles of GS and PLI are provided in Table 1. The IR spectra were simulated using the PDielec package[28] applied to the output of CASTEP

calculations, for a powder of spherical particles diluted in KBr. In order to obtain the decoupled force constants from the DFT calculated vibrational spectra, the verbosity of the CASTEP output was set to 3, and the Cremer–Kraka transformation, as provided by the PyMOL plugin LmodeA-nano[29] was used. For the charge density calculations, spin–orbit couplings were included in the calculations. After applying the den2vasp utility to convert the CASTEP charge density to the VASP CHGCAR format, the Bader analysis program was used to perform Bader charge analysis.[30]

References

1 J. Popp, T. Riggenmann, D. Schröder, T. Ampßler, P. Salvador and P. Klüfers, *Inorg. Chem.*, 2021, **60**, 15980–15996.
2 Rigaku Oxford Diffraction (2019). CrysAlisPro, version 1.171.38.46. Rigaku Oxford Diffraction, Yarnton, UK.
3 G. M. Sheldrick, *Acta Cryst. A*, 2015, **71**, 3–8.
4 G. M. Sheldrick, *Acta Cryst. C*, 2015, **71**, 3–8.
5 O. V. Dolomanov, L. J. Bourhis, R. J. Gildea, J. A. K. Howard and H. Puschmann, *J. Appl. Crystallogr.*, 2009, **42**, 339–341.
6 S. Pillet, in *Structures on Different Time Scales*, eds. T. Woike and D. Schaniel, De Gruyter, 2018, pp. 143–220.
7 G. Te Velde, F. M. Bickelhaupt, E. J. Baerends, C. Fonseca Guerra, S. J. A. Van Gisbergen, J. G. Snijders and T. Ziegler, *J. Comput. Chem.*, 2001, **22**, 931–967.
8 M. Ernzerhof and G. E. Scuseria, *J. Chem. Phys.*, 1999, **110**, 5029–5036.
9 E. Van Lenthe and E. J. Baerends, *J. Comput. Chem.*, 2003, **24**, 1142–1156.
10 J. Li, G. Schreckenbach and T. Ziegler, *J. Am. Chem. Soc.*, 1995, **117**, 486–494.
11 A. Rosa, E. J. Baerends, S. J. A. Van Gisbergen, E. Van Lenthe, J. A. Groeneveld and J. G. Snijders, *J. Am. Chem. Soc.*, 1999, **121**, 10356–10365.
12 R. L. Martin, *J. Chem. Phys.*, 2003, **118**, 4775–4777.
13 F. Neese, *WIREs Comput. Mol. Sci.*, 2022, **12**, e1606.
14 A. D. Becke, *J. Chem. Phys.*, 1993, **98**, 5648–5652.
15 F. Weigend and R. Ahlrichs, *Phys. Chem. Chem. Phys.*, 2005, **7**, 3297.
16 C. Van Wüllen, *J. Chem. Phys.*, 1998, **109**, 392–399.
17 C. Casadevall, V. Martin-Diaconescu, W. R. Browne, S. Fernández, F. Franco, N. Cabello, J. Benet-Buchholz, B. Lassalle-Kaiser and J. Lloret-Fillol, *Nat. Chem.*, 2021, **13**, 800–804.
18 D. Vantelon, N. Trcera, D. Roy, T. Moreno, D. Mailly, S. Guilet, E. Metchalkov, F. Delmotte, B. Lassalle, P. Lagarde and A.-M. Flank, *J. Synchrotron Radiat.*, 2016, **23**, 635–640.
19 K. M. Padden, J. F. Krebs, C. E. MacBeth, R. C. Scarrow and A. S. Borovik, *J. Am. Chem. Soc.*, 2001, **123**, 1072–1079.
20 B. Hu, J. Lu, W. Ding, Y. Liu, M. H. Shroyer, C. E. Schulz, W. Xu, J. Wang and J. Li, *Inorg. Chem.*, 2024, **63**, 18379–18388.
21 S. J. Clark, M. D. Segall, C. J. Pickard, P. J. Hasnip, M. I. J. Probert, K. Refson and M. C. Payne, *Z. Krist.*, 2005, **220**, 567–570.
22 C. J. Pickard and F. Mauri, *Phys. Rev. B*, 2001, **63**, 245101.
23 J. P. Perdew, K. Burke and M. Ernzerhof, *Phys. Rev. Lett.*, 1996, **77**, 3865–3868.
24 E. V. Lenthe, E. J. Baerends and J. G. Snijders, *J. Chem. Phys.*, 1993, **99**, 4597–4610.
25 A. A. Mikhailov, T. Woike, A. Gansmüller, D. Schaniel and G. A. Kostin, *Spectrochim. Acta A*, 2021, **263**, 120217.

26 H. J. Monkhorst and J. D. Pack, *Phys. Rev. B*, 1976, **13**, 5188–5192.
27 A. Tkatchenko and M. Scheffler, *Phys. Rev. Lett.*, 2009, **102**, 073005.
28 J. Kendrick and A. D. Burnett, *J. Comput. Chem.*, 2016, **37**, 1491–1504.
29 Y. Tao, W. Zou, S. Nanayakkara and E. Kraka, *J. Chem. Theory Comput.*, 2022, **18**, 1821–1837.
30 M. Yu and D. R. Trinkle, *The Journal of Chemical Physics*, 2011, **134**, 064111.